Monthly Notices of the ROYAL ASTRONOMICAL SOCIETY
MNRAS **502,** 1026–1040 (2021) doi:10.1093/mnras/staa3896

Mapping the spectral index of Cassiopeia A: evidence for flattening from radio to infrared

V. Domček [1,2★] J. Vink [1,2,3] J. V. Hernández Santisteban [4] T. DeLaney[5] and P. Zhou [1]

[1]*Anton Pannekoek Institute for Astronomy, University of Amsterdam, Science Park 904, NL-1098 XH Amsterdam, the Netherlands*
[2]*GRAPPA, University of Amsterdam, Science Park 904, NL-1098 XH Amsterdam, the Netherlands*
[3]*SRON, Netherlands Institute for Space Research, Sorbonnelaan 2, 3584 CA, Utrecht, the Netherlands*
[4]*SUPA, Physics and Astronomy, University of St Andrews, St Andrews, KY16 9SS, Scotland, UK*
[5]*Physics and Engineering Department, West Virginia Wesleyan College, Buckhannon, WV 26201, USA*

Accepted 2020 December 13. Received 2020 November 25; in original form 2020 May 26

ABSTRACT

Synchrotron radiation from supernova remnants is caused by electrons accelerated through diffusive shock acceleration (DSA). The standard DSA theory predicts an electron spectral index of $p = 2$, corresponding to a radio spectral index of $\alpha = -0.5$. An extension of DSA theory predicts that the accelerated particles change the shock structure, resulting in a spectrum that is steeper than $p > 2$ ($\alpha < -0.5$) at low energies and flattens with energy. For Cassiopeia A, a synchrotron spectral flattening was previously reported for a small part of the remnant in the mid-infrared regime. Here, we present new measurements for spectral flattening using archival radio (4.72 GHz) and mid-infrared (3.6 μm) data, and we produce a complete spectral index map to investigate the spatial variations within the remnant. We compare this to measurements of the radio spectral index from *L*-band (1.285 GHz) and *C*-band (4.64 GHz) maps. Our result shows overall spectral flattening across the remnant ($\alpha_{\text{R-IR}} \sim -0.5$ to -0.7), to be compared with the radio spectral index of $\alpha_{\text{R}} = -0.77$. The flattest values coincide with the locations of most recent particle acceleration. In addition to overall flattening, we detect a relatively steeper region in the south-east of the remnant ($\alpha_{\text{R-IR}} \sim -0.67$). We explore whether these locally steeper spectra could be the result of synchrotron cooling, which provides constraints on the local magnetic field strengths and the age of the plasma, suggesting $B \lesssim 2$ mG for an age of 100 yr, and even $B \lesssim 1$ mG using the age of Cas A, in agreement with other estimates.

Key words: acceleration of particles – radiation mechanisms: non-thermal – ISM: individual objects: Cassiopeia A – ISM: supernova remnants.

1 INTRODUCTION

Cosmic rays (CRs) are highly energetic particles that were discovered more than a century ago (Hess 1912) and they span the energy range from a few hundred MeV up to 10^{20} eV. Their spectral distribution up to 3×10^{15} eV is roughly a power law with a negative index of 2.7. The spectral break around 3×10^{15} eV is known as the 'knee'. Up to this knee, the CR spectrum is dominated by protons, and the CRs must be of Galactic origin (e.g. Hillas 2005). For a long time, it was suspected that the energy needed to accelerate these Galactic CRs was powered by supernovae (Baade & Zwicky 1934). The later identification of radio-synchrotron emission from accelerated electrons in supernova remnants (SNRs) suggested that CR acceleration was taking place in SNRs rather than during the explosion itself (e.g. Ginzburg & Syrovatskii 1964).

The relativistic CR electrons produce radio synchrotron emission (for a review, see Dubner & Giacani 2015) and some young SNRs even produce X-ray synchrotron radiation near their shock fronts (for reviews, see Reynolds 2008; Helder et al. 2012). The gamma-ray detection for many SNRs has confirmed the presence of CRs. The gamma-rays could either be caused by the same electron population that causes synchrotron emission, or could arise from hadronic CRs, which produce gamma-rays through interactions with the background gas. The latter case has been positively identified in at least a few SNRs (e.g. Ackermann et al. 2013). There is not yet evidence that SNRs can accelerate up to the 'knee', but some SNRs can produce CRs close to that energy. For example, the gamma-ray bright source RX J1713.7–3946 produces gamma-rays up to 100 TeV (Aharonian et al. 2007).

The CR acceleration in SNRs is thought to be caused by diffusive shock acceleration (DSA), also known as first-order Fermi acceleration (Axford, Leer & Skadron 1977; Krymskii 1977; Bell 1978; Blandford & Ostriker 1978). According to the DSA theory, charged particles can repeatedly scatter across the shock due to the magnetic field irregularities present on both sides of the shock, thereby gaining energy. After each cycle, a small fraction of the particles will not return to the shock again. The combination of these two effects results in a power-law distribution with a (negative) spectral index of $p = 2$ for the expected compression ratio $\chi = 4$ between shocked and unshocked medium. It was soon realized that if CR acceleration is efficient, the presence of CRs ahead of the shock will influence the unshocked plasma: that is, the CRs will push against the unshocked plasma, compressing it and setting it in

★ E-mail: vdomcek@gmail.com

motion (Eichler 1979; Ellison & Eichler 1984). Moreover, the escape of the highest-energy CRs far ahead of the shock will drain energy from the system. The net result is that the combined compression of the CR precursor and the shock compression itself will be larger than $\chi = 4$, whereas the shock compression itself might be reduced as the flow will arrive at the shock with a slower speed and, therefore, lower Mach number. These processes are addressed in the theory of non-linear DSA (for a review, see Malkov & Drury 2001).

According to the theory of non-linear DSA, the CR spectrum will be steeper than $p = 2$ for low-energy particles, as a result of the lower shock compression, and it will be flatter than $p = 2$ for the highest-energy particles, as these sample the total compression ratio. In the most extreme forms of the theory, the total compression ratio can be larger than 10 (e.g. Baring et al. 1999; Ellison, Berezhko & Baring 2000), largely driven by very high CR acceleration efficiency of > 50 per cent. Indeed, there is some evidence that the radio emission from young SNRs has the predicted deviation from the power law (e.g. concave spectrum; Reynolds & Ellison 1992). The asymptotic value for the spectral index is expected to be $p = 1.5$ (Malkov 1997).

The CRs in the precursor can also give rise to another non-linear effect: they can cause magnetic field amplification through the so-called Bell mechanism (Bell 2004). X-ray synchrotron emission provides evidence of amplified magnetic fields near SNR shocks (Vink & Laming 2003; Helder & Vink 2008).

In recent years, less attention has been paid to the non-linear DSA theory. First of all, although there is some evidence for enhanced compression ratios (Warren et al. 2005), the enhancement seems to be modest (see also Ferrand & Marcowith 2010). Secondly, gamma-ray measurements indicate that the CR acceleration efficiency is not as high as 50 per cent or more, but of the order of 10 per cent (Slane et al. 2014), and for Cassiopeia A it is even as low as 3–6 per cent of the kinetic energy (Araya & Cui 2010). Finally, the gamma-ray spectra of SNRs are more consistent with $p = 2.2$ all the way up to the TeV regime (e.g. Ahnen et al. 2017), instead of the predicted $p = 1.5$.

Cas A is among the youngest known SNRs ($\approx$340 yr; Thorstensen, Fesen & van den Bergh 2001) and the brightest SNR in the sky at radio wavelengths. For this reason, it has played an important role in the debate about the Galactic origin of CRs. Its radio spectrum is steep compared with other young SNRs, $\alpha = -0.77$ (e.g. Baars et al. 1977; Trotter et al. 2017), whereas other young SNRs have $\alpha \approx -0.6$. The radio spectral index is related to the electron spectral index p_e as $\alpha = (p_e - 1)/2$. So, for Cas A, $p_e = 2.54$. This suggests that the spectrum of Cas A has been potentially affected by non-linear DSA effects. For comparison, the general SNR population has, on average, $\alpha \approx -0.5$ (Green 2019), consistent with $p = 2$ predicted by DSA in the absence of non-linear effects (Bell 1978; Malkov & Drury 2001).

If the steep radio spectrum of Cas A is a signature of non-linear DSA, the synchrotron spectrum is expected to flatten at very high frequencies. Indeed, some flattening is reported for the total source spectrum at 247 GHz (Mezger et al. 1986), and up to 550 Hz based on *Planck* data (Onić & Urošević 2015). In addition, two studies of infrared data have also reported that the synchrotron spectrum could be flattening up to 10^{13} Hz (Jones et al. 2003; Rho et al. 2003).

Here, we revisit the case for the flattening of the Cas A spectrum, using archival *Spitzer* 3.6-μm data, which are relatively free of warm dust emission. We combine these data with a 4.72-GHz Very Large Array (VLA) radio map (Thompson et al. 1980), in order to obtain the average spectral index between the two wavelength bands. Our aim was to look specifically for the spatial variation of the spectral index at high frequencies. This is also of interest because Cas A appears to accelerate electrons at both the forward and reverse shocks, as indicated by the association of X-ray synchrotron filaments with both shock regions (Helder & Vink 2008). Moreover, the effects of non-linear DSA (i.e. the flattening spectrum) should at some point be reversed by the effect of the synchrotron energy losses of the highest-energy electrons. In particular, a cooling (or age) break is expected where the cooling time of the electrons equals the age of the source, resulting in an overall break of the spectrum of $\Delta\alpha = 0.5$ (e.g. Longair 2011). The frequency of the cooling break depends on the age and magnetic field of the plasma, which for Cas A is estimated to be around 0.5 mG, but it is likely that variations will be present (Rosenberg 1970; Atoyan et al. 2000; Vink & Laming 2003). This puts the expected cooling break in the mid- to near-infrared regime, as we discuss in Section 4.3.

2 OBSERVATIONS AND DATA ANALYSIS

2.1 Infrared

Infrared data were observed in 2009 August (ObsID 34836224; PI: R. G. Arendt) using the *Spitzer* Infrared Array Camera (IRAC; Fazio et al. 2004) and obtained from the *Spitzer* Heritage Archive. We used the mosaiced products of the extended pipeline (level 2) that combines individual calibrated frames with the refined telescope pointing. For reasons explained at the end of this section, we restrict ourselves to the channel 1 (3.6 μm) data, which have a spatial resolution of 2–2.5 arcsec (Ennis et al. 2006). These data contain the flux measurements (Fig. 1) and their uncertainties, both with pixel sizes of 0.6 arcsec.

2.1.1 Infrared corrections and the Monte Carlo uncertainty propagation

The infrared data require several corrections so that they can be used meaningfully in the analysis. We correct for the infrared environmental background, the point-source contribution from the stars, the extinction in the line of sight, and contributions from the other sources of emission. Each correction of our analysis introduces additional uncertainties. We show the individual contributing steps in Fig. 2.

To tackle all of these contributions, their uncertainties and inter-dependences, we employ Monte Carlo simulations to propagate the uncertainties and to assess their effects on our final spectral index map product. This method has a few advantages over using the analytical/semi-analytical method, as it accounts for a skewness in the distributions and allows for a better propagation of uncertainties. We use 10 000 simulation points. For clarity, we show the applied procedure for a single pixel in Appendix A.

The process starts with a random generation of a normal distribution of the infrared flux for each pixel based on the flux and uncertainty provided by the data.

The first correction we consider is the infrared background, visible in the uncorrected map of the remnant (right panel of Fig. 1). We use regions in the south-west and north-west of Cas A to estimate the level of the background, assumed to be uniform across the remnant. We find that the average flux density per pixel is $\approx 1.00 \times 10^{-5}$, with a 1σ uncertainty of 0.15×10^{-5} Jy px^{-1}. Based on this, we simulate a normal distribution using the Monte Carlo method, which we subtract from the infrared flux distributions. However, as Cas A is located in a complex environment (e.g. structures east and west of the remnant), we also test how an increase of the estimated uncertainty to 0.30×10^{-5} Jy px^{-1} affects the significance of our results.

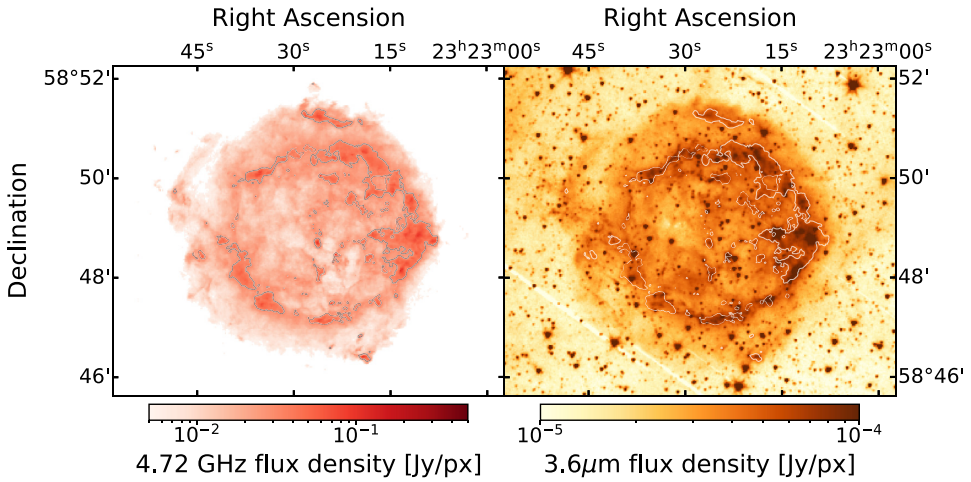

Figure 1. Flux density maps of Cas A. Left: 4.72-GHz image as obtained by the VLA in 2001 (Delaney 2004) and flux calibrated to year 2009 (see Section 2.2.1 for more details). Right: *Spitzer* 3.6-μm image as observed by the PI Arendt in 2009. Radio contours with flux density 0.03 Jy px^{-1} are displayed.

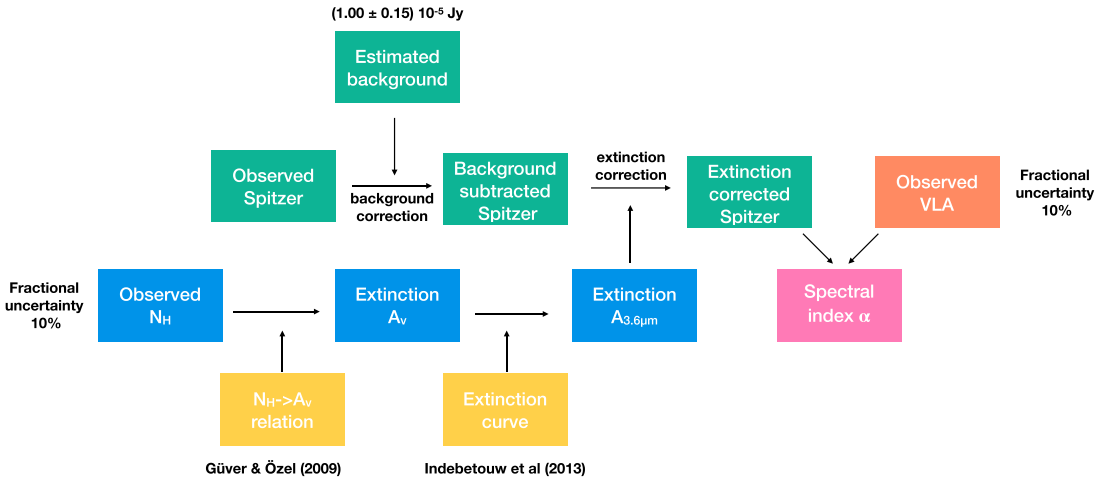

Figure 2. Procedure for obtaining the spatially dependent spectral index $\alpha_{\text{R-IR}}$. Each block represents a separate uncertainty that enters the analysis and is propagated using Monte Carlo simulations towards the final result shown in Fig. 5. The colour-coding points to different data sets from which they arise and is defined as follows: *Spitzer* data (green), Chandra data (blue), VLA data (orange), equations used in the process (yellow) and final spectral index (pink). This colour-coding is further used in Appendix A.

The second consideration in our method is taking into account the infrared extinction. Hurford & Fesen (1996) found extinction in Cas A to be varying in the range $4.6 < A_v < 6.2$ mag, increasing towards the west of the remnant. A recent X-ray study measuring the hydrogen column density (Hwang & Laming 2012) further confirmed these results and use of the Güver & Özel (2009) $N_{\rm H}-A_v$ relation places a lower limit of the extinction at $A_v = 5$ mag. The western part of the remnant shows even stronger extinction with values going up to $A_v = 15$ mag. We use the $N_{\rm H}$ measurements of Hwang & Laming (2012) and assume a 10 per cent fractional uncertainty in each pixel as this uncertainty was not provided. Also in this case, we generate normal distributions and subject the outcome to the $N_{\rm H}-A_v$ relation of Güver & Özel (2009, equation 1)

$$N_{\rm H}\,({\rm cm}^{-2}) = (2.21 \pm 0.09) \times 10^{21} A_v\,({\rm mag}). \quad (1)$$

In order to further transform optical extinction (A_v) into our required wavelength ($A_{3.6\,\mu{\rm m}}$), we relate the optical extinction to K-band extinction using $A_v/A_K = 8.8$ (appropriate for the case of $R_v = 3.1$; Cardelli, Clayton & Mathis 1989). To convert A_K to $A_{3.6\,\mu{\rm m}}$, we use the extinction curve of Indebetouw et al. (2005, equation 4)

$$\log(A_\lambda/A_K) = 0.61(\pm0.04) - 2.22(\pm0.17)[\log(\lambda)] + 1.21(\pm0.23)[\log(\lambda)]^2 \quad (2)$$

to obtain the final extinction map (Fig. 3) and apply it to the *Spitzer* data set.

Stars provide an additional infrared background source in the image. Their presence can increase the measured flux density, and locally change the measured spectral index. Initially, we tried to subtract the point sources using the DAOPHOT extension of the IRAF data reduction software (Tody 1986). This approach was working reliably for the lower flux stars but turned out to be problematic for bright and saturated stars, where the point-source model could not reliably match the data. Additionally, false detections in the filamentary shock structure caused non-affected regions to be altered (Fig. B1). For these reasons, we decided to exclude and mask the brighter stars instead of subtracting them. Nevertheless, we still made

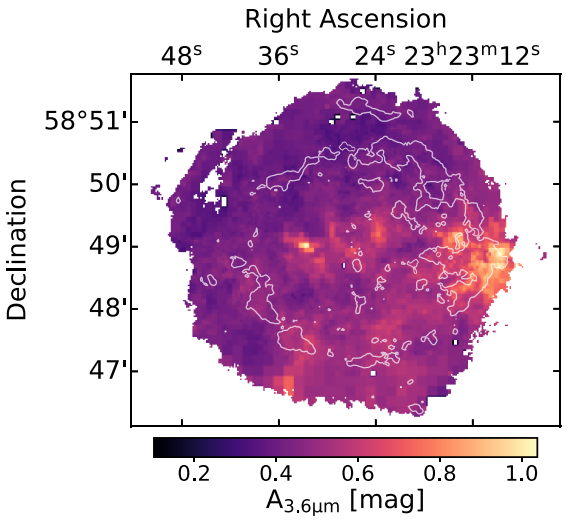

Figure 3. Extinction correction map at 3.6 μm based on X-ray $N_{\rm H}$ measurements (Hwang & Laming 2012).

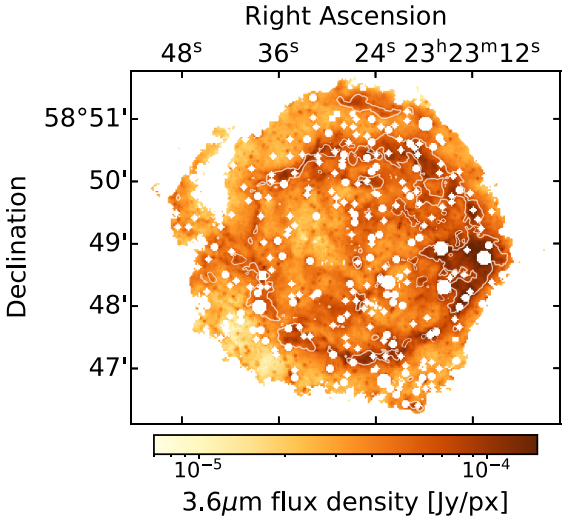

Figure 4. *Spitzer* 3.6-μm observation after background subtraction and extinction correction with the star mask applied. The radio contour level 3×10^{-2} Jy px^{-1} is displayed for easier orientation.

use of the point-source subtracted map to make the lower-resolution spectral index map in Section 3.3.

Masking was performed using DAOStarFinder.[1] A few of the lower flux stars are still present in the final image but, because of their size and low-flux nature, they do not significantly affect our analysis.

Another source of emission that usually contributes to infrared wavelengths is thermal emission from dust particles. Based on the size and chemical composition of the dust particles, radiation can be produced in different wavelengths covering different *Spitzer* channels. Dust in Cas A consists mostly of silicate dust (De Looze et al. 2017) and, because of the radiative properties of silicon grain, its contribution below $\lambda \sim 7$ μm is suppressed considerably (see fig. 10 of Draine & Li 2007, and fig. 3 of Rho et al. 2008).

[1]https://photutils.readthedocs.io/en/stable/api/photutils.detection.DAOStarFinder.html

There are other potential emission features at wavelengths shorter than 7 μm. Most noticeably, Ennis et al. (2006) suggested that [Fe II] could be contributing to channel 3 up to 50 per cent of its detected flux, and Rho et al. (2012) reported the detection of the molecular double-peaked CO line emission in the ∼4.2−5.0 μm range, which is covered by *Spitzer* channel 2. The energy range of channel 1 could also contain the contribution of polycyclic aromatic hydrocarbons (PAHs) but, as shown in fig. 2 of Reach et al. (2006), these are not relevant for Cas A. Channel 1 is therefore the only channel that appears to be dominated by synchrotron radiation, and its synchrotron origin is supported by several previous studies (Jones et al. 2003; Rho et al. 2003; Ennis et al. 2006). Therefore, we choose only channel 1 ($\lambda \simeq 3-4$ μm) of the *Spitzer* data for our analysis. The background- and extinction-corrected map is shown in Fig. 4. For a more in-depth discussion on the origin of the emission in each of the *Spitzer* channels, we refer the reader to Ennis et al. (2006).

2.2 Radio

2.2.1 High-resolution 4.72-GHz image

For the construction of the high-resolution radio-to-infrared spectral index map, we used a 4.72-GHz VLA radio image obtained in 2000–2001 (Delaney 2004). We performed the flux calibration by fitting a power law of the flux density measurements from Perley & Butler (2017) and obtaining the flux density at 4.72 GHz. For the total flux density to correspond with the year when *Spitzer* data were obtained (2009), this value was further corrected for the secular fading using decline rate of 0.67 per cent yr^{-1}, reported by Trotter et al. (2017). The total flux density of Cas A after these corrections is $S_{4.72\,\rm GHz}$ = 697.6 Jy. Additionally, we apply a low flux density mask to the data, which masks out flux densities lower than 5×10^{-3} Jy px^{-1} corresponding to the background level and masks out regions that reach more than 10 per cent of the thermal noise contribution. The beam size of the observation is an ellipse with a major axis of 0.3792 arcsec, a minor axis of 0.3333 arcsec, and a position angle of 90°. The original map has an image pixel size of 0.1 arcsec. We assume a fractional uncertainty of 10 per cent in the flux for each pixel as an upper limit of uncertainty for our radio data.

2.2.2 Additional radio data

In order to have a reference radio spectral index map to investigate the flattening, we also obtained the VLA *L*-band and *C*-band flux density images from DeLaney et al. (2014), where the data calibration and image preparation is described in full. The *C*-band image was normalized to 4.64 GHz and the *L*-band image was normalized to 1.285 GHz. The original images at 2.5-arcsec resolution have a low dynamic range as reported in DeLaney et al. (2014), which results in poor quality spectral index maps. Therefore, the flux density images were Gaussian smoothed to a resolution of 10 arcsec to improve the signal-to-noise ratio for spectral index measurements. Because these flux density images are co-eval, there is no need to normalize them to the scale used by Perley & Butler (2017). The uncertainty in the integrated flux density at each band is about 2 per cent for the 1997–1998 observation epoch (Perley & Taylor 1991).

2.3 Spectral index maps

The creation of spectral index maps is one of the main methods used to investigate the spectral evolution of extended objects such as SNRs. The core of this method is to compare flux measurements

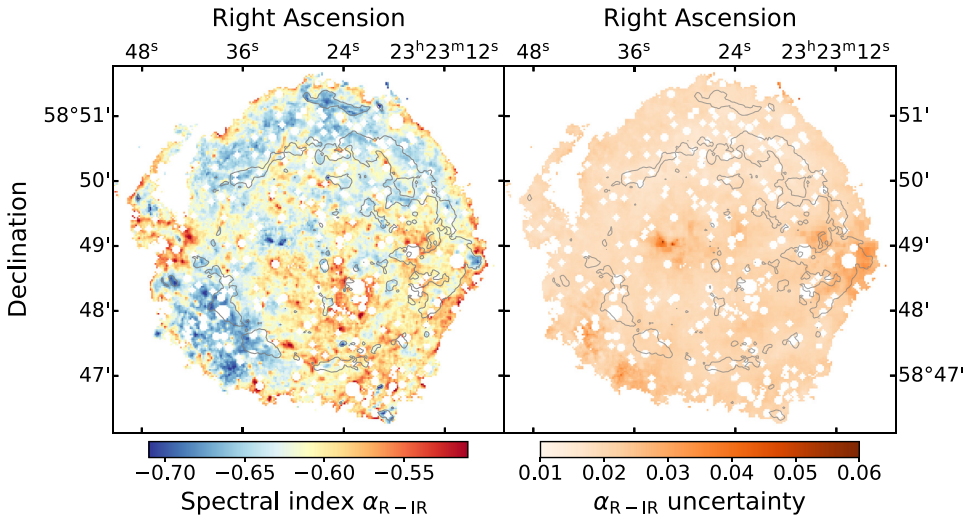

Figure 5. Radio to mid-infrared spectral index map (left) with its uncertainties (right). The radio contour level of 3×10^{-2} Jy px^{-1} is displayed for easier orientation.

at two distinct frequencies. The further these frequencies are apart, the less dependent the measure spectral index is on systematic and statistical uncertainties of the flux measurements. In order to make the spectral index maps, we first co-align radio and infrared images to the same coordinate grid with a pixel size of ≈ 1.4 arcsec px^{-1}. We use the `reproject_exact` tool in Python[2] to achieve this.

We produce two spectral index maps using the following equation:

$$\alpha = \frac{\log(S_{\nu_2}) - \log(S_{\nu_1})}{\log(\nu_2) - \log(\nu_1)}. \quad (3)$$

The radio-to-infrared spectral index map is constructed between the VLA (4.72 GHz) and the *Spitzer* (3.6 μm) bands. Here, S_{ν_1} and S_{ν_2} correspond to calibrated flux per pixel in the radio and the infrared, respectively, while ν_1 and ν_2 are the corresponding frequencies of the input maps. Note that S_{ν_2} was subjected to our Monte Carlo method for obtaining uncertainty distributions. We collapse these results into two maps that show the median spectral index value and its 1σ uncertainty in Fig. 5.

The reference radio–radio spectral index map between the *u–v* matched lower-resolution 1.285 GHz and the 4.64-GHz flux density images was computed using the AIPS task COMB. In order to ensure that the spectral index between the two radio images is robust, a number of techniques were employed as described in DeLaney et al. (2014). The most important of these is the use of the same 4.64-GHz image as a default when using the AIPS maximum entropy deconvolution routine VTESS to make the final 1.285- and 4.64-GHz flux density images (Cornwell & Evans 1985). For weak radio sources, calibration errors that are caused by, for example, slightly different *u–v* coverage of the radio observations and slightly different primary beam attenuation corrections can lead to spurious spectral index measurements. However, Cas A is exceptionally bright and therefore the minor differences in the primary beam have very little effect and the strict matching of *u–v* coverage is not required to obtain reliable spectral index measurements. Although the nominal spatial resolution of the 1.285- and 4.64-GHz flux density images is 2.5 arcsec based on *u–v* coverage, The two flux density images were also Gaussian smoothed to 10-arcsec resolution to improve the signal-to-noise ratio and to allow reliable spectral index measurements even in fainter regions.

[2]https://reproject.readthedocs.io/en/stable/api/reproject.reproject_exact.html

3 RESULTS

We produced spectral index maps between the radio (4.72 GHz) and infrared (3.6 μm) – see Fig. 5 – and between two radio frequencies (1.285 and 4.64 GHz). The results show an overall significant flattening of the average radio spectral index $\alpha_R = -0.7653 \pm 0.0002$ to the radio-infrared index $\alpha_{R\text{-}IR} = -0.6143 \pm 0.0002$.

3.1 Radio-to-infrared spectral index

Fig. 5 shows that the radio-to-infrared spectral index map has some structure to it, although in all cases the spectral index is flatter than the average radio spectral index of $\alpha_R \approx -0.77$.

The flattest index (with values of $\alpha_{R\text{-}IR} \approx -0.60$) is found in the outer rim regions close to the forward shock and over the majority of the south-western quadrant of the remnant. The index steepens slightly to $\alpha_{R\text{-}IR} \approx -0.62$ between the forward and reverse shocks, most visibly in the northern half of the remnant. The region that stands out most in the radio-to-infrared spectral index map is located in the south-eastern part of the remnant and has a relatively steep spectral index of $\alpha_{R\text{-}IR} \approx -0.66$. This relatively steep spectral index is at least partially caused by the lack of emission in the mid-infrared band, which is also noticeable in the other *Spitzer* channels (4.5, 5.8 and 8.0 μm) and in the X-ray non-thermal emission (Helder & Vink 2008). The available portion of this region in the radio spectral index map in Fig. 6 also appears to be steeper, although the difference from the mean radio spectral index is smaller than in the mid-infrared case.

In order to compare these interesting regions with the results for the whole remnant, we produce separate histograms for some regions and calculate their mean spectral index in flux density space. For a clear display of the results, we specify the regions as the outer rim (in pink), the northern arc (blue), the south-east (purple) and the south-west (green). We show their locations in Fig. 7. Also, we list the mean values in Table 1, and show the respective histograms in Fig. 8 (left).

We tested whether or not we are over-subtracting the background in the remnant by performing our analysis on one of the low-flux

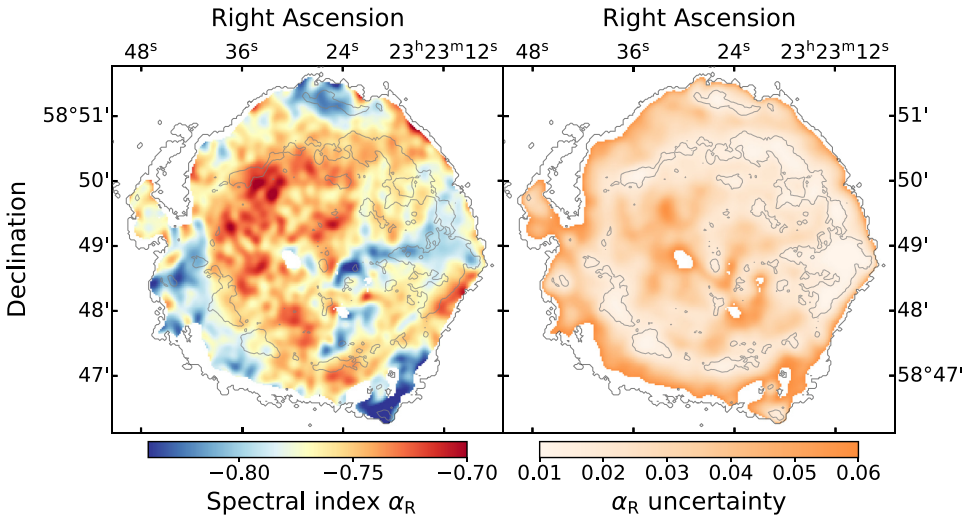

Figure 6. Radio spectral index between *L*-band (1.285 GHz) and *C*-band (4.64 GHz) based on the 1997/1998 radio data of DeLaney et al. (2014) (left). Uncertainty of the radio spectral index (right). In addition to radio contours of flux density 0.03 Jy px^{-1}, we also display the outer boundary of the radio-to-infrared spectral index map from Fig. 5.

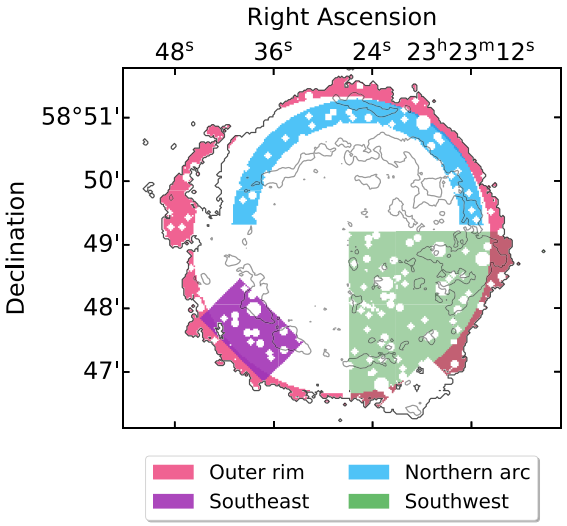

Figure 7. Masking regions used for regions of interest in Table 1.

pixels in the south-east region. We find that, even in this low-flux region, the flux is still sufficient for the background correction to proceed and produce a Gaussian-shaped distribution (see Fig. A1).

We further tested the effect of increasing the uncertainty of the background to 3×10^{-5} Jy px^{-1}. Although it does not change the spectral index values by itself, it can, in the most affected low mid-infrared flux regions, increase the uncertainty up to 0.06. However, this still points towards significant enough spectral flattening.

3.2 Radio spectral index

The lower-resolution radio spectral index map (Fig. 6) portrays a slightly different picture compared with the radio-to-infrared spectral index. The mean radio spectral index for the whole remnant is 0.7653 ± 0.0002, which is in agreement with the previously measured values of Baars et al. (1977) and Trotter et al. (2017). However, in terms of the spatial distribution, flatter indices appear mainly in the centre east, turning into steeper values in the west. Between the forward and reverse shocks, the situation appears to be similar to $\alpha_{\text{R-IR}}$ where we observe close to average or slightly steeper values in locations we call the northern arc and south-east. Unfortunately, because of the limits of the radio images we cannot reliably construct the pixel-to-pixel spectral index in the outer rim region. We can nevertheless compute the mean spectral index from the radio flux density maps, which points towards similar steeper values as between the shocks.

The tip of the south-west region shows steep radio spectral index values. This region corresponds to one of the locations where the supernova shock wave has overrun a slow-moving optical knot (Braun, Gull & Perley 1987; Anderson et al. 1991), resulting in a bow shock. The interaction caused rapid brightening in the 1970s and consequent fading since the 1980s. However, the radio-to-infrared spectral index does not show any noticeable steepening within the same region. It is possible that the steep index in radio comes from a different electron population that is superimposed on top of the underlying typical average region.

Table 1 summarizes the mean radio spectral indices for all selected regions from Fig. 7.

3.3 Spectral index comparison

A comparison of the radio-to-infrared and inter-radio spectral index map can give a more complete picture of the spectral index evolution in the remnant and better point to regions of greater or lesser flattening. For this purpose, we constructed a spectral index deviation map, $\Delta\alpha$ (Fig. 9).

In order to produce the $\Delta\alpha$ map, we required a radio-to-infrared spectral index map with a spatial resolution of 10 arcsec. However, it was not possible to use Gaussian smoothing on the data from Fig. 5 because of the high number of masked point sources in the remnant.

Therefore, we took an alternative approach of producing the radio-to-infrared spectral index map in a lower resolution. We circumvented the issue of the star masking by using a smoothed point-source subtracted map (Figs B1 and B2). Although this approach may have resulted in a partial loss of flux in the filamentary structure as

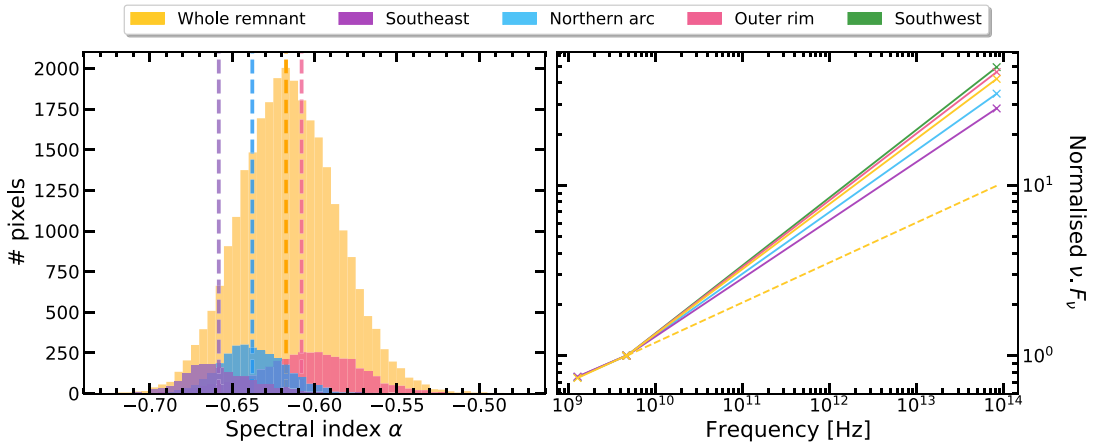

Figure 8. Left: histogram of median spectral index values $\alpha_{\text{R-IR}}$ for regions of interest. The outer rim region appears to be significantly flatter than the northern arc and south-east. Dashed lines represent mean values of individual distributions. Right: spectral energy distribution for the same locations, including the south-west region that has a histogram spread similar to the outer rim. The yellow dashed line shows extrapolation of the mean radio spectral index for the whole remnant at higher frequencies. All regions have been normalized at 4.72 GHz.

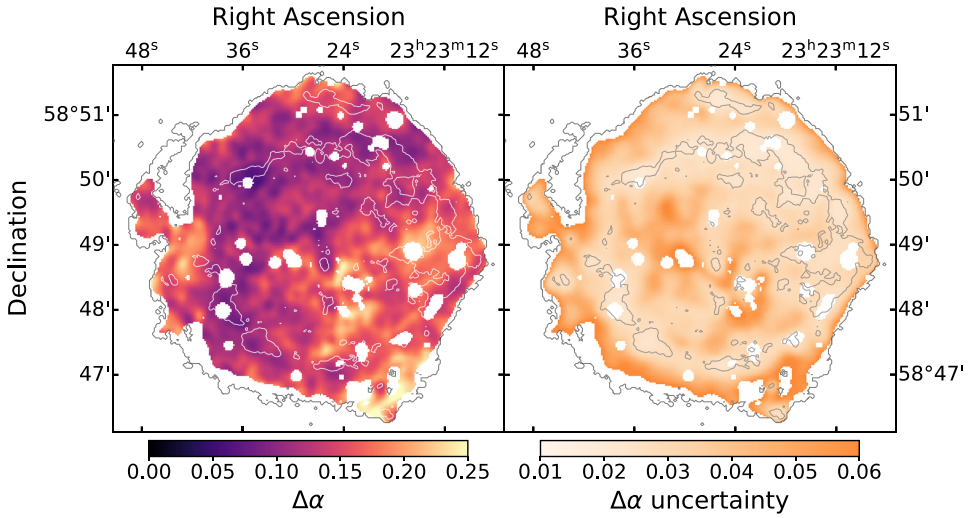

Figure 9. Deviation between the radio spectral index (α_{R}) and radio-to-infrared spectral index ($\alpha_{\text{R-IR}}$). In addition to radio contours of flux density 0.03 Jy px^{-1}, we also display the outer boundary of the radio-to-infrared spectral index map from Fig. 5.

Table 1. Mean spectral indices for regions of interest shown in Fig. 8. α_{R} represents radio spectral index while $\alpha_{\text{R-IR}}$ is the radio-to-infrared spectral index. $\Delta\alpha$ represents the difference between the two indices.

Region	Mean spectral index α_{R}	Mean spectral index $\alpha_{\text{R-IR}}$	Deviation $\Delta\alpha$
Whole remnant	-0.7652 ± 0.0002	-0.6173 ± 0.0002	0.1479 ± 0.0003
Outer rim	-0.7777 ± 0.0009	-0.6078 ± 0.0005	0.170 ± 0.001
Northern arc	-0.7742 ± 0.0006	-0.6378 ± 0.0004	0.1364 ± 0.0007
South-east	-0.7795 ± 0.0009	-0.6581 ± 0.0006	0.121 ± 0.001
South-west	-0.7726 ± 0.0004	-0.6011 ± 0.0004	0.1715 ± 0.0005

a result of false detection of point sources (the reason we do not use this approach in the higher-resolution analysis), the consequent smoothing has largely filled out these over-subtracted locations and spread the possible deficiency of flux over a larger region. A comparison of the two methods shows that the impact on the measured $\alpha_{\text{R-IR}}$ in Table 1 does not deviate more than $\Delta\alpha \approx 0.005$ for any given averaged region.

Additionally, as a few saturated stars were not subtracted correctly, we masked these locations in our lower-resolution spectral index map. We display the point-source subtracted map, smoothed flux images and lower-resolution spectral index map in Appendix B (see Figs B1, B2 and B3).

The final 10-arcsec spectral index deviation map (see Fig. 9) shows flattening everywhere by at least $\Delta\alpha \sim 0.05$. Three regions appear

to be flattening significantly more ($\Delta\alpha > 0.15$) than in the rest of the remnant: the south-west, the east (slightly south-west of the base of the jet) and the north, around the filamentary structure (see Fig. 9).

The south-western quadrant is flattening more as a whole. For the most part, this is a combination of a relatively average index in radio and a much flatter radio-to-infrared index. This quadrant has also stronger X-ray synchrotron continuum emission (see fig. 6 of Helder & Vink 2008). The north location is centred around a bright filamentary structure that is steeper than average in both $\alpha_{\rm R}$ and $\alpha_{\rm R\text{-}IR}$, but still shows an above average flattening. The east location is steep in radio, but flattens considerably towards infrared (Fig. 9). It does not appear to have either the radio filamentary structure or any strong X-ray synchrotron emission as in the previously pointed out location that could explain its flattening. This region contains some of the Fe-rich ejecta that have overtaken the silicon-rich shell, and it does have a relatively high ionization age compared with other parts of the remnant (Hwang & Laming 2012). It is not immediately clear what the connection is between these X-ray determined plasma properties and the radio and radio-to-infrared spectral indices.

In contrast, the south-eastern region in the radio-to-infrared spectral index map does not seem to stand out as much in Fig. 9. It experiences only mild flattening that is comparable to other regions. The region is nevertheless still interesting as, together with the northern filament, both of these locations have steeper than average spectra.

4 DISCUSSION

Our study shows that there is an overall flattening of the synchrotron spectrum of Cas A between radio and infrared. Here we compare our results with previous studies on the broad-band spectral properties of synchrotron emission, and we discuss the results in the context of non-linear shock acceleration models and a possible cooling break.

4.1 Comparison with other studies

Evidence for spectral flattening of the synchrotron spectrum with respect to the radio spectral index measured below 10 GHz has been found previously. High-frequency radio observations above 30 GHz have already shown that the overall spectrum of Cas A flattens at high frequencies (Mezger et al. 1986; Onić & Urošević 2015). This is also supported by infrared studies in the 2-μm range (Jones et al. 2003; Rho et al. 2003). The most important difference between these studies and what is presented here is that the high-frequency radio studies explored the spectral flattening of the whole remnant, without the ability to detect spatial variation across the whole remnant. The infrared study by Jones et al. (2003) was restricted to small regions in the north-west part of the remnant, and the spectral tomography study by Rho et al. (2003) was limited mainly to the bright shell, due to the low flux of diffuse emission in the *K*-band, and the relatively high background.

Moreover, we find, on average, flatter spectral indices ($\alpha_{\rm R\text{-}IR} \sim -0.6$) compared with those reported at 2 μm ($\alpha_{2\,\mu\rm m} \sim -0.7$), even for comparable locations. The discrepancy could be caused either by a general steepening at shorter wavelengths, or by differences in the employed methodology, for example by our more detailed treatment of extinction and uncertainties (see Fig. 2).

As there are some systematic uncertainties regarding the measurements of $N_{\rm H}$ of the order of 25 per cent (see, e.g., Zhou & Vink 2018), we tested the effect of a 25 per cent overestimation of $N_{\rm H}$ in our final spectral index. We found it to be $\Delta\alpha \approx 0.02$ at most, so $N_{\rm H}$ overestimation cannot account for the discrepancy between our measurements and those using the emission at 2 μm.

A general steepening at shorter wavelengths would be an interesting possibility, as it may hint at a synchrotron cooling break, similar to that discussed in Section 4.3.

The relativistic electron population responsible for the synchrotron emission will also produce gamma-ray emission through inverse Compton scattering, with a power-law slope that should be $\Gamma = \alpha + 1$. However, for Cas A, the gamma-ray emission is suspected to be dominated by hadronic gamma-ray radiation: protons and other atomic nuclei colliding with background plasma, thereby producing neutral pions, which immediately decay into photons. If we denote the particle spectral index with p, the gamma-ray spectral index for pion decay should be $\Gamma \approx p$, whereas for inverse Compton scattering it should be $\Gamma = (p + 1)/2$; see Hinton & Hofmann (2009) for a review on the gamma-ray emission from SNRs.

Several studies of the gamma-ray spectrum in the GeV to TeV range covered by *Fermi*-LAT and the VERITAS and MAGIC observatories all find a spectral index for the protons of $p \approx 2.2$ (e.g. Yuan et al. 2013; Ahnen et al. 2017; Abeysekara et al. 2020). According to the DSA theory, both electrons and hadrons are accelerated with the same spectral index in momentum. This also means that they should have the same spectral index in energy, provided the hadrons are relativistic, and the electron spectrum is not affected by synchrotron cooling. So, if the gamma-ray emission from Cas A is hadronic, then the accelerated electrons have the same slope, and we expect a radio spectral index of $\alpha = -(p - 1)/2 = -0.6$. This is indeed consistent with our results, and inconsistent with the spectral index below ∼10 GHz.

4.2 Consequences for the shock acceleration models

The observed flattening of the spectrum from radio to infrared synchrotron radiation is in line with the predictions of non-linear DSA. This theory predicts that the flattening is expected to occur in those electron populations accelerated by the most efficiently accelerating shocks (i.e those shocks capable of converting a large fraction of the shock energy into accelerated particles). Our results indicate that the flattest spectra are located in the south-western quadrant. This is also the location of stronger non-thermal X-ray emission (see fig. 6 of Helder & Vink 2008), where the forward and reverse shocks are closest to each other. It is therefore probably a place of more efficient particle acceleration, which could also exhibit stronger flattening effects. As discussed by Helder & Vink (2008), the western part is also the region where the reverse shock has the highest shock velocity in the frame of the ejecta.

Going from the forward shock inwards into the outer radio shell (northern arc region in Fig. 7), a gradual steepening of indices is observed in the $\alpha_{\rm R\text{-}IR}$ map. This is not as obvious in the $\Delta\alpha$ map, but this map has a lower spatial resolution. The steepening could indicate that, in the past, when this electron population was accelerated, the radio-to-infrared spectrum was steeper, and less affected by non-linear effects. However, because the shock velocity was higher in the past, a more likely explanation is that the steeper spectum has been affected by synchrotron cooling. Moreover, the radio spectral index is typical for Cas A (i.e. $\alpha_{\rm R} \approx -0.77$), which is the reason why non-linear models need to be considered in the first place.

However, the flattest spectral indices that we measure near the shock regions are not supporting the case for the extreme non-linear acceleration, which predicts particle spectral indices $p < 2$ (Malkov 1997), and hence synchrotron spectral indices $\alpha < 0.5$. In more recent updates of the non-linear DSA models (e.g. Vladimirov, Bykov &

Ellison 2008; Caprioli et al. 2009), more emphasis is placed on the effects of magnetic field amplification by the Bell mechanism (Bell 2004) on the energy distribution of the accelerated particles. In a recent paper, Bell, Matthews & Blundell (2019) show that the energy transferred from the accelerating particles to the magnetic field will also lead to steeper particle spectra. Another way in which magnetic fields may affect the particle spectra is if the particles scatter off an Alfvén wave that has an average velocity with respect to the plasma velocity. This can reduce the effective contrast in velocities experienced by the accelerating particles, resulting in steeper spectra (Zirakashvili et al. 2008). Although modification of the non-linear DSA model indeed predicts steeper spectra, the idea that particles of different energy have experienced different shock compression ratios still stands. Thus, the expected result is still a spectrum that is steeper at low energies than at high energies, consistent with our findings.

Note that an altogether different explanation for spectral variation was presented by Atoyan et al. (2000), who suggested a two-zone model when trying to explain the observed flattening in the averaged radio spectra (Mezger et al. 1986). They argued that the flattening is caused by accelerated particles escaping from bright steep-spectrum radio structures (knots, ring) into the diffuse radio 'plateau'. However, this model predicts flatter spectra in the plateau and steeper spectra at the acceleration sites. Our spatially resolved results contradict this model, which shows the opposite to be true.

4.3 Cooling break and the magnetic field

Both the radio-to-infrared spectral index map (Fig. 5) and the index deviation map (Fig. 9) show regions where the flattening is minimal (i.e. $\Delta\alpha \approx 0.05$) and/or the radio-to-infrared spectrum is still relative steep (i.e. $\alpha_{\text{R-IR}} \approx < -0.65$).

There are several possible reasons why the spectrum does not flatten out to $\alpha \gtrsim -0.6$ everywhere. First, the steep spectrum and lack of flattening could be intrinsic to the particle acceleration properties that shaped the spectrum of those regions; for example, stronger magnetic field amplification due to higher shock velocities (Bell et al. 2019) compared with more flattening regions. Secondly, it could be caused by synchrotron cooling, which has steepened the spectrum since the acceleration took place. In this case, the intrinsic concave curvature of the spectrum could be offset by additional steepening at higher frequencies.

Intrinsic differences in concave spectral curvature cannot be ruled out, but it is difficult to attribute these to stronger magnetic field amplification in the steepest regions, as seen in the northern and south-eastern parts of the remnant. If anything, all indications point towards a more efficient acceleration and higher shock velocities being present in the south-west (e.g. Helder & Vink 2008). This is where we encounter the flattest spectra (in agreement with non-linear shock acceleration models), and where the X-ray synchrotron emission is brightest. We cannot exclude the possibility that the situation was different one or two centuries ago, when the bulk of the electrons were accelerated.

Here we discuss the second option – synchrotron cooling – and the implications it might have for the acceleration history and magnetic field strength throughout the remnant. The synchrotron cooling effects are a function of the time since the electrons were first accelerated and the magnetic field strength. Under the assumption of steepening due to synchrotron cooling, this implies that regions with small $\Delta\alpha$ have been shocked earlier, or that the magnetic field strength is higher.

As a reminder, a relativistic electron gyrating around the magnetic field line radiates away its energy within a cooling time-scale

$$\tau_{\text{syn}} \equiv \frac{E}{\mathrm{d}E/\mathrm{d}t} = \frac{9}{4}\frac{(m_{\text{e}}c^2)^4}{e^4 c B^2 E_{\text{e}}} \approx 1250 \left(\frac{E_{\text{e}}}{1\,\text{TeV}}\right)^{-1} \left(\frac{B}{100\,\mu\text{G}}\right)^{-2} \text{yr}, \quad (4)$$

where m_{e} and e are the mass and electrical charge of the electron, E_{e} is its energy, and B is the magnetic field strength.

Equating the synchrotron loss time-scale, τ_{syn}, with the age of the electron population, t_{age}, we obtain the time-dependent energy that represents the turnover energy in the particle spectra. Above this energy, we do not expect to detect any more particles due to synchrotron losses for an accelerated electron population with a single age.

For a given electron energy, the typical synchrotron radiation frequency is (Ginzburg & Syrovatskii 1965)

$$\nu_{\text{syn}} = 4.6 \times 10^{13} \left(\frac{B}{100\,\mu\text{G}}\right) \left(\frac{E_{\text{e}}}{1\,\text{TeV}}\right)^2 \text{Hz}. \quad (5)$$

Combining equation (5) with equation (4) gives the typical frequency above which the synchrotron spectrum should be affected by radiative losses (i.e. the cooling break frequency):

$$\nu_{\text{br}} \approx 7.2 \times 10^{16} \left(\frac{B}{100\,\mu\text{G}}\right)^{-3} \left(\frac{t_{\text{age}}}{100\,\text{yr}}\right)^{-2} \text{Hz}. \quad (6)$$

In a SNR, the total emission arises from a combination of synchrotron cooled spectra with different ages for the electron populations. So, whereas each population will have its own sharp cut-off in frequency, the combination of different populations leads to a broken power-law spectrum, with the break frequency corresponding to the age of the oldest electron population (e.g. Longair 2011), and the break frequency given by equation (6).

4.3.1 *Break frequency estimation*

In order to assess whether a synchrotron cooling break could have affected the average flattening of the spectrum, we need to make an assumption about what the asymptotic spectral index would be without synchrotron cooling.

The principle of our frequency cooling break estimation is sketched in Fig. 10. The three crosses represent the measured fluxes, while α_{R} and $\alpha_{\text{R-IR}}$ are the spectral indices between them. We do not know the true underlying flux distribution. Nevertheless, for the non-linear acceleration, we can generally expect the spectrum to become flatter (harder) before ultimately being driven down by the synchrotron cooling. This is represented by the black curve in Fig. 10.

Our estimate for the frequency at which a cooling break may be present consists of approximating the curved spectrum by two segments with fixed power-law slopes: the flattened spectrum, α_1, and the spectrum affected by the cooling, α_2. These two segments together are forced to be consistent with the average measured spectral index $\alpha_{\text{R-IR}}$. We make an assumption on how flat α_1 can be and we set it as an upper limit. We then extrapolate a line from the last observed radio point to higher frequencies. At a certain frequency, a cooling break occurs and changes the slope of α_1 to the steeper α_2. Here we make another assumption that the change between these two indices is $\delta\alpha = \alpha_1 - \alpha_2 = 0.5$. This assumption is motivated by calculations of continuous injection electron spectra (Longair 2011) and can be taken as a lower limit for the change in the

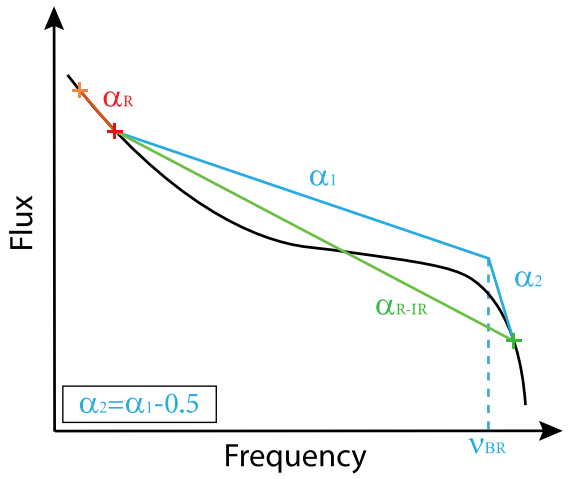

Figure 10. A schematic diagram of what the synchrotron curve may look like, if affected by both non-linear acceleration and synchrotron cooling (solid black curve). The orange, red and green crosses represent the available flux data, while the red and green lines are the measured radio and radio-to-infrared spectral indices. By making an assumption for the maximally flattening α_1 and applying a cooling break $\alpha_2 = \alpha_1 - 0.5$ (blue lines), we estimate the lower limit of frequency where the cooling break occurs.

slope. Note that larger $\delta\alpha$ leads to higher estimations of the cooling break frequency. By requiring the second slope of α_2 to intersect with the infrared flux measurement, we obtain the lower limit of the cooling break frequency.

Using the available data, there are two possible approaches to estimate maximum flattening of α_1. The first approach takes advantage of the histogram in Fig. 8, where we assume that the maximum flattening measured in the remnant ($\alpha_{\rm R\text{-}IR} \approx -0.55$) is the true flattening unaffected by synchrotron cooling everywhere. The $\alpha_{\rm R\text{-}IR} = -0.55$ value is close to the expected α from the test-particle approach ($\alpha \approx -0.50$). Moreover, $\alpha = -0.55$ (corresponding to $p = 2.1$) is consistent with, but somewhat flatter than, the gamma-ray spectral index of $\Gamma \approx 2.2$ (Section 4.1). We estimate the lower limit for the frequency break using equation (7) where α_1 is set to be -0.55 while the flux density S changes depending on the position in the remnant. The break frequency is then given by

$$\nu_{\rm br} = \left(\frac{S_{3.6\,\mu\rm m}}{S_{4.72\,\rm GHz}}\right)^{1/(\delta\alpha)} \left(\frac{\nu_{3.6\,\mu\rm m}}{\nu_{4.72\,\rm GHz}}\right)^{\alpha_1/(\delta\alpha)} \nu_{3.6\,\mu\rm m}, \quad (7)$$

with $\nu_{3.6\,\mu\rm m} = 8.3 \times 10^{13}$ Hz being the central frequency of the *Spitzer* image used.

The resulting map is then used as an input to equation (6) to estimate the upper limit of the magnetic field B.

An alternative way to put constraints on a possible cooling break frequency is to assume that the radio spectra all flatten out with a fixed $\Delta\alpha$, rather than towards a fixed final spectral index α_1. Assuming that the maximal flattening corresponds to a region in the remnant not affected by synchrotron cooling, we used this maximal flattening of $\Delta\alpha = 0.22$ with respect to the radio spectral index (see Fig. 9) for all regions.

This effectively relaxes the condition that every part of the remnant needs to flatten to the same $\alpha_1 = -0.55$, no matter whether it is steeper or flatter in radio, but this forces the use of the lower-resolution map. Using the second option, α_1 in equation (7) is calculated individually for each pixel where $\alpha_1 = \alpha_{\rm R} + \Delta\alpha$.

Both approaches (i.e. left panels of Figs 11 and 12) show qualitatively similar results, although the detailed structures in the maps can differ. Note that both $\alpha_1 = -0.55$ and $\Delta\alpha = 0.22$ are extreme values, resulting in relatively low-frequency limits for the break frequency. In general, the lower-limit estimates for the break frequency are about an order of magnitude below the frequency of the *Spitzer* observation ($\nu_{3.6\,\mu\rm m} = 8.3 \times 10^{13}$ Hz). The lowest possible cooling break frequencies are found (not surprisingly) in the regions of steeper spectra in the east and the north of the remnant. However, in the regions where we detect strong flattening, such as in the south-west, the break frequency is in the vicinity of the *Spitzer* observation, in which case there is effectively no need to invoke a synchrotron cooling break.

We stress here that we do not measure a cooling break frequency, but explore the need for such a frequency under the assumption that the asymptotic spectral index is $\alpha = -0.55$ throughout the remnant, or that all spectra are concave and flatten by $\alpha = 0.22$.

As such, we offer a first attempt to map out the cooling break in the remnant. The results suggest that, if the spectrum has a cooling break below or near the infrared map, the lowest frequency of the cooling break is to be found in the south-east and north-east locations. Whether the steeper spectra there are indeed caused by synchrotron cooling needs to be further investigated. However, it is difficult to directly map synchrotron radiation at lower frequencies, because of the thermal emission from dust grains. So the best option would be to obtain deep near-infrared imaging. Indeed, the 2-μm measurements by Rho et al. (2003) provide a hint that the synchrotron spectrum is generally steepening with respect to our measurements at 8.3×10^{13} Hz.

4.3.2 *Magnetic field*

Assuming that the steeper spectra found in the south-east and north-eastern regions are caused by synchrotron cooling, we can explore the implications for the local magnetic field strengths, using equation (6) to transform the limit on $\nu_{\rm br}$ into an upper limit of the magnetic field strength. However, this requires knowledge of when the radiating plasma was shocked. We used $t_{\rm age} = 100$ yr in the maps presented in the right panels of Figs 11 and 12 mostly for convenience. This places the magnetic field upper limit as high as 2–2.5 mG in the most affected regions, while most flattening parts of the remnant in the south-east do not allow magnetic field values to rise beyond 1 mG. These magnetic field upper limits are in general higher than magnetic field estimates in the literature, although Atoyan et al. (2000) did invoke local magnetic field strengths as high as 2 mG. By using a plasma age of 100 yr, we strike a compromise between the maximum age, corresponding to the age of Cas A (∼340 yr), and the other extreme (i.e. having plasma with electrons accelerated during the era of radio observations).

The latter option (i.e. $\tau_{\rm age} < 50$ yr) seems too extreme, given that the earliest radio-synthesis maps of Cas A (in the early 1960s; Ryle, Elsmore & Neville 1965) show that the overall morphology of Cas A has not changed dramatically over the last 50 yr. So, at worst, the upper limits would be 60 per cent higher, if we assume the unlikely case of $\tau_{\rm age} = 50$ yr.

However, it is entirely possible that a dominant fraction of the remnant's plasma was shocked in the first century after the explosion. In that case, we could use the age of Cas A, which is about ∼340 yr. This scales down the magnetic field upper limit in the right panels of Figs 11 and 12 by a factor of 2.2, bringing the upper limits down to 0.45–1 mG.

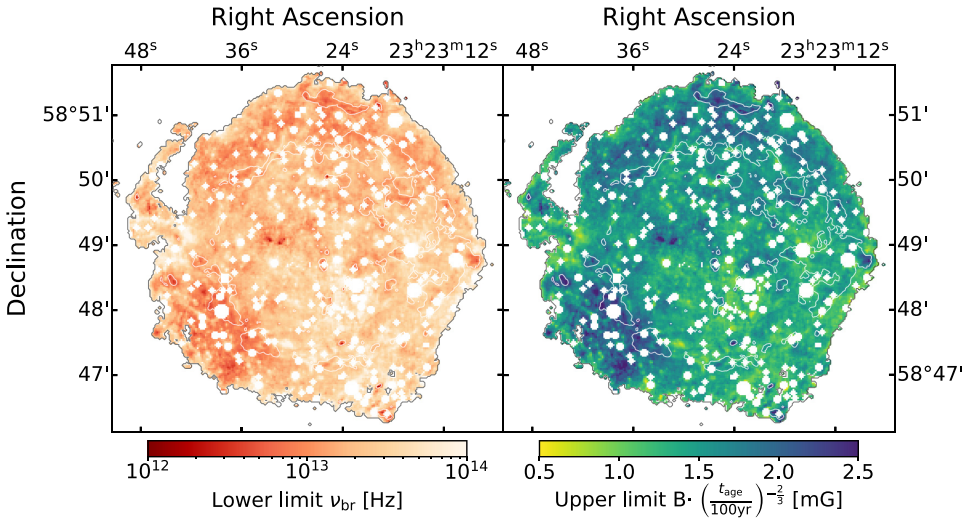

Figure 11. Estimate of the synchrotron spectrum frequency break lower limit (left) and magnetic field upper limit (right) with $\alpha_1 = -0.55$. In addition to radio contours of flux density 0.03 Jy px^{-1}, we also display the outer boundary of the radio-to-infrared spectral index map from Fig. 5.

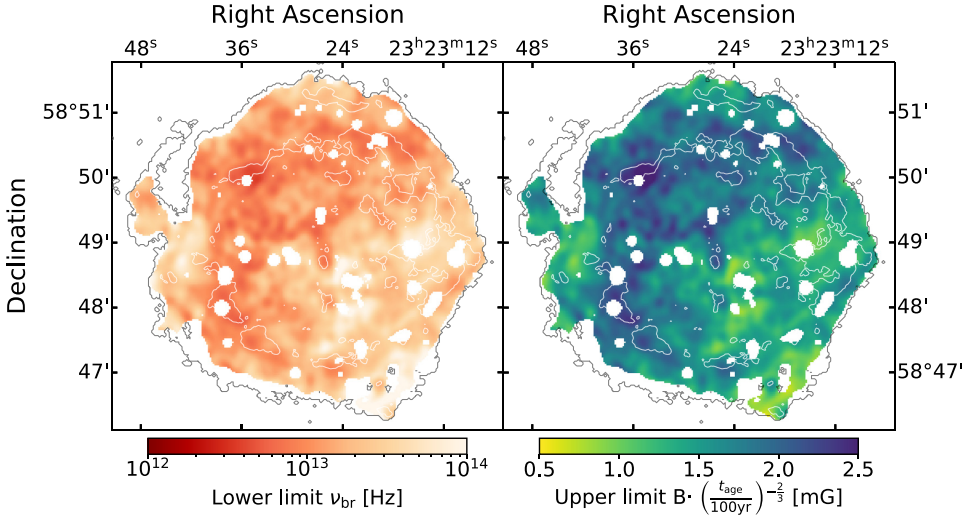

Figure 12. Estimate of the synchrotron spectrum frequency break lower limit (left) and magnetic field upper limit (right) with $\alpha_1 = \alpha_R + \Delta\alpha$. In addition to radio contours of flux density 0.03 Jy px^{-1}, we also display the outer boundary of the radio-to-infrared spectral index map from Fig. 5.

These magnetic field upper limits are consistent with other estimates of the magnetic field strength for Cas A. Near the shock fronts, X-ray synchrotron observations provide estimates of the magnetic field strengths of 100–500 μG (Vink & Laming 2003; Berezhko & Völk 2004; Bamba et al. 2005; Ballet 2006; Helder et al. 2012). Joint modelling of the broad-band spectral energy distribution of the non-thermal radiation (radio, X-rays and gamma-rays) also suggests magnetic fields of $\gtrsim$150 μG (Atoyan et al. 2000; Ahnen et al. 2017; Abeysekara et al. 2020). Finally, early estimates of the overall magnetic field strength based on the minimum energy argument were ∼500 μG (Rosenberg 1970).

The fact that our location-dependent magnetic field upper limits are consistent with overall estimates of the magnetic fields in Cas A adds credibility to the idea that the steeper spectra are indeed affected by synchrotron cooling. Clearly, follow-up studies are needed to confirm this. This is important because this is one of the few observational methods that can inform us about the acceleration history of the relativistic electron populations in Cas A.

5 CONCLUSIONS

We investigated the spatially dependent spectral changes in synchrotron emission by comparing high spatial resolution radio (4.72 GHz) and infrared (3.6 μm) maps of Cas A. For the first time, we obtain a spectral index map between these two bands. The aim was to verify earlier reports that the the non-thermal spectrum of Cas A is flattening, consistent with predictions from non-linear DSA theory. Unlike previous studies, we obtain a spatial map of spectral indices, after correcting for interstellar extinction and testing for potential systematic errors. We also compare with the radio (1.285–4.64 GHz) spectral index map.

Our main findings are the following.

(i) We observe flattening of the non-thermal spectrum all across the whole remnant with an average radio to mid-infrared spectral index $\alpha_{\text{R-IR}} = -0.61$. This is approximately $\Delta\alpha \simeq 0.15$ flatter than the measured average spectral index in radio $\alpha_R \sim -0.765$.

(ii) The flattest indices are obtained at the locations of assumed active particle acceleration with high shock velocities, such as near the forward shock and the south-west quadrant of the remnant. These locations also coincide with the regions that are brightest in non-thermal X-ray emission.

(iii) The flattening of the spectrum at high frequencies is in qualitative agreement with non-linear DSA theory. The spectral index is, however, still steeper than the predictions of the non-linear models without magnetic field amplification (see Malkov & Drury 2001, and references therein).

(iv) We assess the possibility of a cooling break being present in the remnant. We place the break frequency lower limit at $\nu_{\rm br} \sim 5 \times 10^{12}$ Hz in the likely most affected regions. Considering 100 yr as the age of the shocked plasma, this indicates allowed magnetic field strength up to $B \sim 2$–2.5 mG in the south-east/north-east and $B \sim 1$ mG in the south-west of the remnant. This is higher than the average magnetic field limits inferred for Cas A, but probes the magnetic field values suggested locally by Atoyan et al. (2000). Using the age of Cas A (∼340 yr) as the age of the plasma puts the upper limits close to the magnetic field estimates obtained with other methods. Further investigations are still necessary and south-east/north-east regions are the best candidate locations for further investigation of the cooling break. Doing this may put constraints on the history of electron acceleration in Cas A.

ACKNOWLEDGEMENTS

The work of VD is supported by a grant from the NWO graduate programme/GRAPPA-PhD programme. JVHS acknowledges support from the STFC grant ST/R000824/1. We would like to thank Una Hwang for providing the $N_{\rm H}$ maps, and Matthew Baring and Dan Milisavljevic for their insights. This work is based in part on observations made with the *Spitzer Space Telescope*, which was operated by the Jet Propulsion Laboratory, California Institute of Technology under a contract with NASA.

This research made use of ASTROPY, a community-developed core Python package for astronomy (Astropy Collaboration 2013) and MATPLOTLIB (Hunter 2007). We further made use of SAOIMAGE DS9 (Joye & Mandel 2003), PYRAF (Science Software Branch at STScI 2012) and NASA's Astrophysics Data System.

DATA AVAILABILITY

The data underlying this article are available from the Zenodo repository, at https://doi.org/10.5281/zenodo.4478615.

REFERENCES

Abeysekara A. U. et al., 2020, ApJ, 894, 51
Ackermann M. et al., 2013, Science, 339, 807
Aharonian F. et al., 2007, A&A, 464, 235
Ahnen M. L. et al., 2017, MNRAS, 472, 2956
Anderson M., Rudnick L., Leppik P., Perley R., Braun R., 1991, ApJ, 373, 146
Araya M., Cui W., 2010, ApJ, 720, 20
Astropy Collaboration, 2013, A&A, 558, A33
Atoyan A. M., Tuffs R. J., Aharonian F. A., Völk H. J., 2000, A&A, 354, 915
Axford W. I., Leer E., Skadron G., 1977, in Proc. 15th International Cosmic Ray Conference. Dept. of Cosmic Rays, Central Research Institute for Physics of the Hungarian Academy of Sciences, Budapest, p. 132
Baade W., Zwicky F., 1934, Proceedings of the National Academy of Sciences, 20, 259
Baars J. W. M., Genzel R., Pauliny-Toth I. I. K., Witzel A., 1977, A&A, 500, 135
Ballet J., 2006, Advances in Space Research, 37, 1902
Bamba A., Yamazaki R., Yoshida T., Terasawa T., Koyama K., 2005, ApJ, 621, 793
Baring M. G., Ellison D. C., Reynolds S. P., Grenier I. A., Goret P., 1999, ApJ, 513, 311
Bell A. R., 1978, MNRAS, 182, 147
Bell A. R., 2004, MNRAS, 353, 550
Bell A. R., Matthews J. H., Blundell K. M., 2019, MNRAS, 488, 2466
Berezhko E. G., Völk H. J., 2004, A&A, 419, L27
Blandford R. D., Ostriker J. P., 1978, ApJ, 221, L29
Braun R., Gull S. F., Perley R. A., 1987, Nature, 327, 395
Caprioli D., Blasi P., Amato E., Vietri M., 2009, MNRAS, 395, 895
Cardelli J. A., Clayton G. C., Mathis J. S., 1989, ApJ, 345, 245
Cornwell T., Evans K., 1985, A&A, 143, 77
De Looze I., Barlow M. J., Swinyard B. M., Rho J., Gomez H. L., Matsuura M., Wesson R., 2017, MNRAS, 465, 3309
Delaney T. A., 2004, PhD thesis, Univ. Minnesota
DeLaney T., Kassim N. E., Rudnick L., Perley R. A., 2014, ApJ, 785, 7
Draine B. T., Li A., 2007, ApJ, 657, 810
Dubner G., Giacani E., 2015, A&A Rev., 23, 3
Eichler D., 1979, ApJ, 229, 419
Ellison D. C., Eichler D., 1984, ApJ, 286, 691
Ellison D. C., Berezhko E. G., Baring M. G., 2000, ApJ, 540, 292
Ennis J. A., Rudnick L., Reach W. T., Smith J. D., Rho J., DeLaney T., Gomez H., Kozasa T., 2006, ApJ, 652, 376
Fazio G. G. et al., 2004, ApJS, 154, 10
Ferrand G., Marcowith A., 2010, A&A, 510, A101
Ginzburg V., Syrovatskii S., 1964, The Origin of Cosmic Rays. Elsevier, Amsterdam
Ginzburg V. L., Syrovatskii S. I., 1965, ARA&A, 3, 297
Green D. A., 2019, J. Astrophys. Astron., 40, 36
Güver T., Özel F., 2009, MNRAS, 400, 2050
Helder E. A., Vink J., 2008, ApJ, 686, 1094
Helder E. A., Vink J., Bykov A. M., Ohira Y., Raymond J. C., Terrier R., 2012, Space Science Reviews, 173, 369
Hess V. F., 1912, Physik. Zeitschr., 13, 1084
Hillas A. M., 2005, J. Phys. G: Nucl. Part. Phys., 31, R95
Hinton J., Hofmann W., 2009, ARA&A, 47, 523
Hunter J. D., 2007, Comput. Sci. Eng., 9, 90
Hurford A. P., Fesen R. A., 1996, ApJ, 469, 246
Hwang U., Laming J. M., 2012, ApJ, 746, 130
Indebetouw R. et al., 2005, ApJ, 619, 931
Jones T. J., Rudnick L., DeLaney T., Bowden J., 2003, ApJ, 587, 227
Joye W. A., Mandel E., 2003, in Payne H. E., Jedrzejewski R. I., Hook R. N., eds, ASP Conf. Ser. Vol. 295, Astronomical Data Analysis Software and Systems XII. Astron. Soc. Pac., San Francisco, p. 489
Krymskii G., 1977, Akademiia Nauk SSSR Doklady, 234, 1306
Longair M. S., 2011, in Longair M. S., ed., High Energy Astrophysics, 3rd edn. Cambridge Univ. Press, Cambridge( )
Malkov M. A., 1997, ApJ, 485, 638
Malkov M. A., Drury L. O., 2001, Reports on Progress in Physics, 64, 429
Mezger P., Tuffs R., Chini R., Kreysa E., Gemuend H., 1986, A&A, 167, 145
Onić D., Urošević D., 2015, ApJ, 805, 119
Perley R. A., Butler B. J., 2017, ApJS, 230, 7
Perley R. A., Taylor G. B., 1991, AJ, 101, 1623
Reach W. T. et al., 2006, AJ, 131, 1479
Reynolds S. P., 2008, ARA&A, 46, 89
Reynolds S. P., Ellison D. C., 1992, ApJ, 399, L75
Rho J., Reynolds S. P., Reach W. T., Jarrett T. H., Allen G. E., Wilson J. C., 2003, ApJ, 592, 299
Rho J. et al., 2008, ApJ, 673, 271
Rho J., Onaka T., Cami J., Reach W. T., 2012, ApJ, 747, L6
Rosenberg I., 1970, MNRAS, 151, 109
Ryle M., Elsmore B., Neville A. C., 1965, Nature, 205, 1259
Science Software Branch at STScI, 2012, pyRAF: Python alternative for IRAF. Astrophysics Source Code Library, record ascl:1207.011

Slane P., Lee S-H., Ellison D. C., Patnaude D. J., Hughes J. P., Eriksen K. A., Castro D., Nagataki S., 2014, ApJ, 783, 33
Thompson A. R., Clark B. G., Wade C. M., Napier P. J., 1980, ApJS, 44, 151
Thorstensen J. R., Fesen R. A., van den Bergh S., 2001, AJ, 122, 297
Tody D., 1986, in Crawford D. L., ed., Proc. SPIE Conf. Ser. Vol. 0627, Instrumentation in Astronomy VI. SPIE, Bellingham, p. 733
Trotter A. S. et al., 2017, MNRAS, 469, 1299
Vink J., Laming J. M., 2003, ApJ, 584, 758
Vladimirov A. E., Bykov A. M., Ellison D. C., 2008, ApJ, 688, 1084
Warren J. S. et al., 2005, ApJ, 634, 376
Yuan Y., Funk S., Jóhannesson G., Lande J., Tibaldo L., Uchiyama Y., 2013, ApJ, 779, 117
Zhou P., Vink J., 2018, A&A, 615, A150
Zirakashvili V. N., Ptuskin V. S., 2008, in Aharonian F. A., Hofmann W., Rieger F., eds, AIP Conf. Ser. Vol. 1085. Am. Inst. Phys., New York, p. 336

APPENDIX A: EXAMPLE OF OBTAINING SPECTRAL INDICES PER PIXEL USING MONTE CARLO SIMULATIONS

In order to illustrate our procedure for measuring a spectral index for a single pixel and to prove the overall robustness of our results given the statistical and systematic errors, we show here our procedure for a given pixel, and how it leads to a likelihood range in the spectral index.

We chose a pixel in the south-east location at coordinates (RA 23h 23m 39^{s}.1, Dec. 58 47′ 23″.8) as our example pixel to provide a more complete picture of our data-handling process. The location is ideal to showcase the effect of the strongest effect of background subtraction as this region provides the lowest mid-infrared flux.

We use a Monte Carlo approach in order to propagate the uncertainties and to obtain the result. The basis of this method is to take a value and its uncertainty of a given parameter and to simulate a normal distribution around it. In our case, we produce one-dimensional arrays of 10 000 elements. These arrays are then used as input into equations as if it would be a single value. However, as we do it on 10 000 elements we are saving the information about parameter's possible values and effectively we also propagate its uncertainty.

A.1 Background subtraction

The flux in the chosen pixel is 190.1 $\times$ 10^{-7} Jy px^{-1} with an uncertainty 9.1 $\times$ 10^{-7} Jy px^{-1}. The mid-infrared background value was estimated to be 1.0 $\pm$ 0.15 $\times$ 10^{-5} Jy px^{-1}. Using the Monte Carlo technique, we produce a normal distribution array with

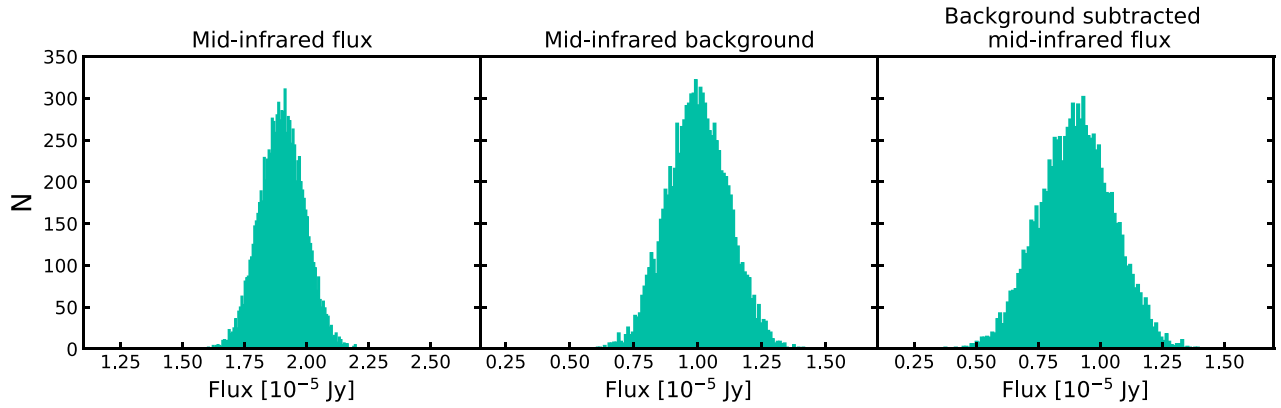

Figure A1. *Spitzer* background correction process. Left and middle images show simulated normal distributions for *Spitzer* data for a given pixel and estimated global mid-infrared background, respectively. Right: final background-subtracted distribution. Colour-coding refers to Fig. 4.

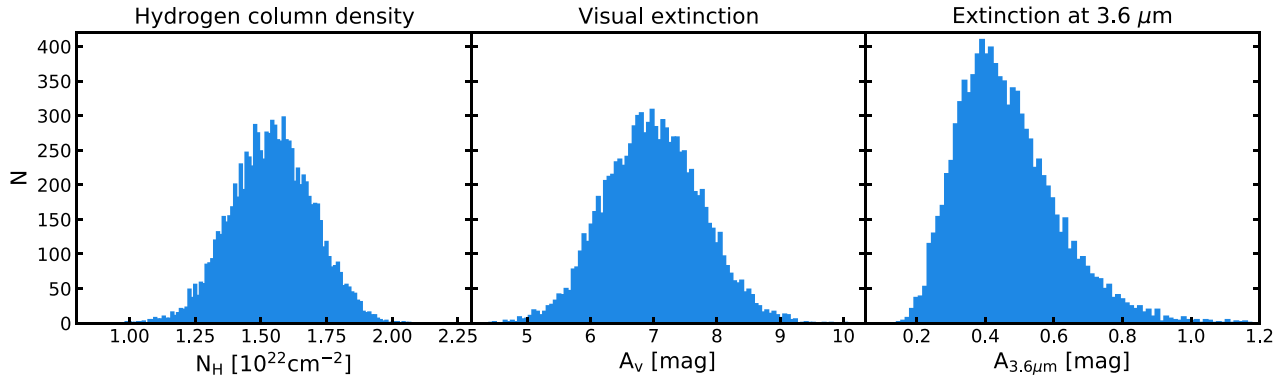

Figure A2. Extinction conversion process from hydrogen column density measured in X-rays into extinction at 3.6 μm. Left: distribution simulated from X-ray N_H data. Middle: distribution after conversion to visual magnitude A_v (using Güver & Özel 2009, equation 1). Right: distribution adapted to 3.6-μm extinction (using Indebetouw et al. 2005, equation 4). Colour-coding refers to Fig. 4.

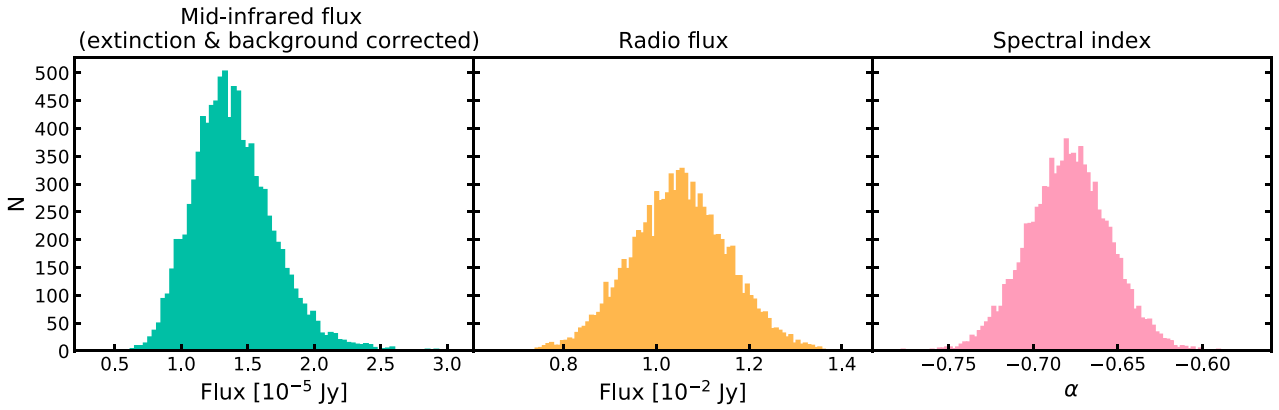

Figure A3. Obtaining the final power-law index. Left: background- and extinction-corrected distribution. Middle: simulated distribution based on radio data. Right: final spectral index distribution for the given pixel. Colour-coding refers to Fig. 4.

10 000 values of both mid-infrared flux (Fig. A1, left) and estimated background (Fig. A1, centre).

The background-subtracted distribution (Fig. A1, right) is produced by subtraction of these two arrays and has a Gaussian shape. This is a result that should be expected if the background correction is applied correctly. If we were over-subtracting the background, the distribution would be cut from the left side and would introduce inaccuracy and bias into our method. As we chose a pixel in the low-flux south-eastern region, this is additional proof that the steeper values we see there are not caused by over-subtraction.

A.2 Extinction calculation

We obtain an extinction value from the X-ray measurements of hydrogen column density $N_{\rm H}$ provided by Hwang & Laming (2012). For our chosen pixel, $N_{\rm H}$ is 1.54×10^{22} cm^{-3}. Because the uncertainty is not available, we assume that it is 10 per cent of the $N_{\rm H}$ value. The simulated distribution of the 10 000 $N_{\rm H}$ values (Fig. A2, left) is converted into visual extinction A_v (Fig. A2, centre) by propagating through the $N_{\rm H}$–A_v relation from equation (1) of Güver & Özel (2009) and further transformed to extinction at 3.6 μm (Fig. A2, right) using the extinction curve from equation (4) of Indebetouw et al. (2005); see also equations (1) and (2) of this paper for convenience.

In this conversion, we also accounted for the uncertainties in relations between $N_{\rm H}$, $A_{\rm V}$ and the final extinction at 3.6 μm. The resulting extinction distribution has a longer tail in higher extinction values. This is a product of unequal uncertainties in the relation of the extinction curve and would be much harder to account for analytically. The distribution's shape is still approximately Gaussian. The obtained extinction distribution is then applied to mid-infrared data using the Pogson equation, resulting in the distribution shown in Fig. A3 (left).

A.3 Spectral index

The final step is combining the background- and extinction-corrected distribution of mid-infrared flux (Fig. A3, left) with the radio data (Fig. A3, centre) by propagating it through equation (3). The radio flux for the given pixel is 1.05×10^{-2} Jy px^{-1}. As the uncertainty was not available, we assumed that it was 10 per cent of the flux. The final result also has a Gaussian shape and is shown in the right panel of Fig. A3.

APPENDIX B: SPECTRAL INDEX ANALYSIS IN LOWER RESOLUTION

In order to construct the spectral index deviation map, $\Delta\alpha$, in Fig. 9, it was necessary to create a spectral index map at a lower resolution. We used DAOPHOT to subtract the stars in the 3.6-μm *Spitzer* data (Fig. B1), combined with the 4.72-GHz map smoothed to 10-arcsec resolution (Fig. B2). The final low-resolution spectral index map $\alpha_{\rm R\text{-}IR}$ is shown in Fig. B3. A detailed explanation of the procedure is presented in Sections 2.1.1 and 3.3.

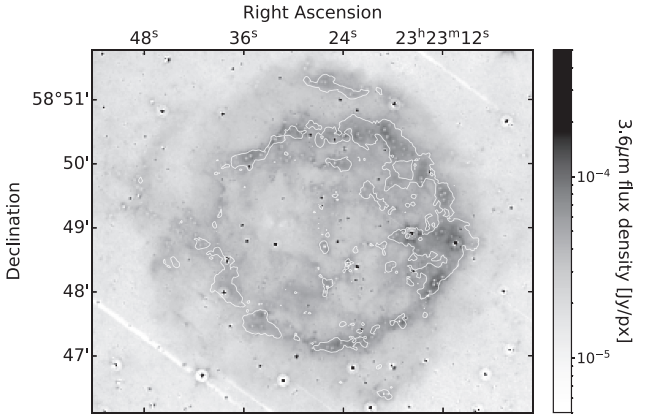

Figure B1. Point-source subtracted *Spitzer* 3.6-μm image from Fig. 1 (right). White point sources show partially over-subtracted stars while black point sources were too bright or saturated to be subtracted correctly. Radio contours with flux density 0.03 Jy px^{-1} are displayed.

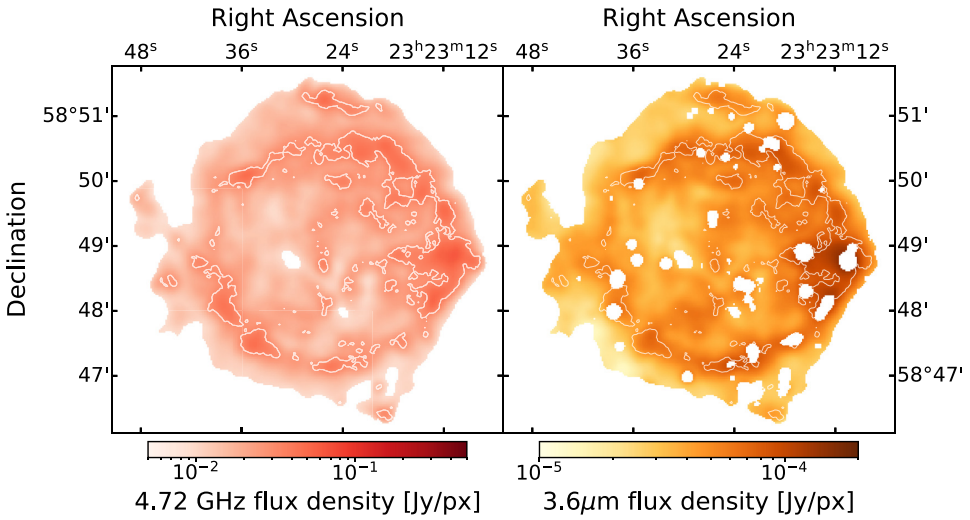

Figure B2. Flux density maps of Cas A used for construction of the $\Delta\alpha$ map in Fig. 9. Left: smoothed 4.72-GHz image from Fig. 1 (left). Right: star and background subtracted, extinction-corrected and smoothed *Spitzer* 3.6-μm image from Fig. 1 (right). Radio contours with flux density 0.03 Jy px^{-1} are displayed.

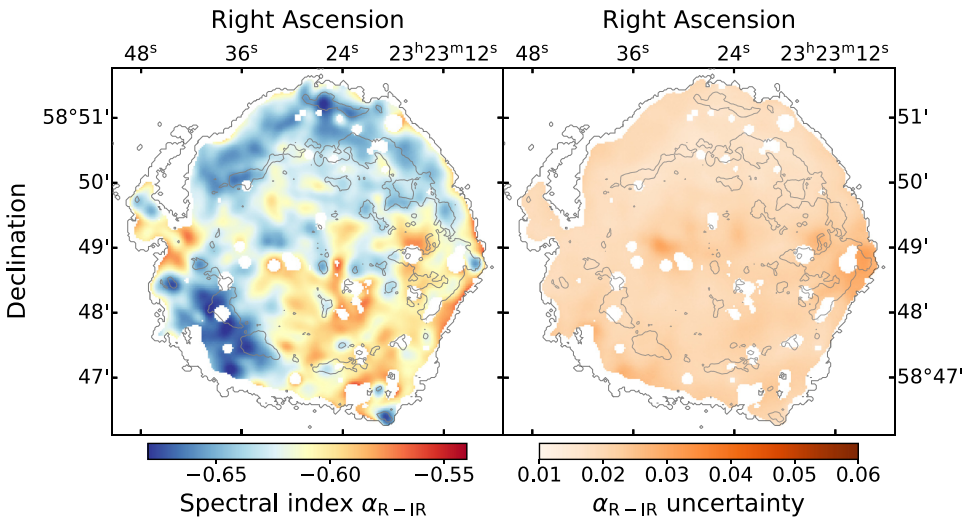

Figure B3. Radio-to-infrared spectral index map made in the 10-arcsec spatial resolution. This map is used for construction of the spectral index difference map in Fig. 9. In addition to radio contours of flux density 0.03 Jy px^{-1}, we also display the outer boundary of the radio-to-infrared spectral index map from Fig. 5.

This paper has been typeset from a TEX/LATEX file prepared by the author.